# Uncovering axionlike particles in supernova gamma-ray spectra

Francesca Calore,[1,*] Pierluca Carenza,[2,†] Christopher Eckner,[1,3,‡] Maurizio Giannotti,[4,§] Giuseppe Lucente,[5,6,‖] Alessandro Mirizzi,[5,6,¶] and Francesco Sivo[5,6,**]

[1]*LAPTh, CNRS, F-74000 Annecy, France*
[2]*The Oskar Klein Centre, Department of Physics, Stockholm University, Stockholm 106 91, Sweden*
[3]*LAPP, CNRS, F-74000 Annecy, France*
[4]*Physical Sciences, Barry University, 11300 NE 2nd Ave., Miami Shores, Florida 33161, USA*
[5]*Dipartimento Interateneo di Fisica "Michelangelo Merlin", Via Amendola 173, 70126 Bari, Italy*
[6]*Istituto Nazionale di Fisica Nucleare—Sezione di Bari, Via Orabona 4, 70126 Bari, Italy*

(Received 14 June 2023; accepted 23 January 2024; published 7 February 2024)

A future Galactic supernova (SN) explosion can lead to a gamma-ray signal induced by ultralight axionlike particles (ALPs) thermally produced in the SN core and converted into high-energy photons in the Galactic magnetic field. The detection of such a signal is in the reach of the Large Area Telescope aboard the Fermi Gamma-Ray Space Telescope. The observation of gamma-ray emission from a future SN has a sensitivity to $g_{a\gamma} \gtrsim 4 \times 10^{-13}$ GeV$^{-1}$ for a SN at fiducial distance of 10 kpc and would allow us to reconstruct the ALP-photon coupling within a factor of ∼2, mainly due to the uncertainties on the modeling of the Galactic magnetic field.

DOI: 10.1103/PhysRevD.109.043010

## I. INTRODUCTION

The detection of gamma-ray signals in coincidence with a Galactic core-collapse (CC) supernova (SN) explosion has been pointed out as smoking-gun signature associated with the emission of novel particles, like axions [1–8], heavy sterile neutrinos [9–11], or dark photons [12]. In this context, one of the most studied possibilities is the case of ultralight axionlike particles (ALPs), coupled with photons through the coupling $g_{a\gamma}$, that would be thermally produced in the SN core via the Primakoff process [1,2]. These ALPs are expected to freely escape from the SN core and travel through the Galactic magnetic field, converting into photons, and potentially generating an unexpected gamma-ray burst simultaneously with the neutrino signal.

A notable application of this mechanism is the strong bound, $g_{a\gamma} \lesssim 4.2 \times 10^{-12}$ GeV$^{-1}$ for $m_a < 4 \times 10^{-10}$ eV [7], from the lack of a gamma-ray signal in the gamma-ray spectrometer on the Solar Maximum Mission in coincidence with the neutrino signal from SN 1987A (see also [3] for a previous estimation of the bound). The physics potential of current gamma-ray detectors has been extensively explored in the past few years. In particular, it was shown that if a Galactic SN were to explode during the lifetime of the Large Area Telescope aboard the Fermi satellite (hereinafter Fermi-LAT), one could probe the ALP parameter space significantly below the previous constraints, with a sensitivity down to $g_{a\gamma} \gtrsim 2 \times 10^{-12}$ GeV$^{-1}$ for ultralight ALPs and a SN placed in the Galactic Center [13]. Furthermore, a search for gamma-ray bursts from extragalactic SNe with Fermi-LAT has yielded the limit $g_{a\gamma} < 2.6 \times 10^{-11}$ GeV$^{-1}$, for ALP masses $m_a < 3 \times 10^{-10}$ eV, under the assumption of at least one SN occurring in the detector field of view [14]. Finally, the cumulative emission of ALPs from all past CC SNe in the Universe would produce a diffuse ALP flux, whose conversion into photons in the Galactic magnetic field can lead to a potentially detectable diffuse gamma-ray flux at MeV energies. Using recent measurements of the diffuse gamma-ray flux observed by Fermi-LAT one can set the bound $g_{a\gamma} \lesssim 3.8 \times 10^{-11}$ GeV$^{-1}$ for $m_a \ll 10^{-11}$ eV [5,15].

In this paper, we explore the sensitivity of Fermi-LAT to the detection of a gamma-ray signal induced by ALPs emitted from a Galactic SN. In particular, we will demonstrate that a detection of such a signal, in coincidence with the SN neutrino burst, would represent a hint for new physics, providing a unique opportunity to reveal the existence of ALPs and precisely reconstruct their properties, such as the ALP-photon coupling and the average energy of their spectrum.[1]

*calore@lapth.cnrs.fr
†pierluca.carenza@fysik.su.se
‡eckner@lapth.cnrs.fr
§mgiannotti@barry.edu
‖giuseppe.lucente@ba.infn.it
¶alessandro.mirizzi@ba.infn.it
**francesco.sivo@ba.infn.it

[1]Following a similar rationale, some of the authors have analyzed the sensitivity to heavy, MeV-scale, ALPs from SNe in Ref. [8].

 © 2024 American Physical Society

Our work follows this structure. In Sec. II, we characterize the initial SN ALP flux, the ALP-photon conversion in the Galactic magnetic field and the observable gamma-ray flux. In Sec. III, we assess the capability of Fermi-LAT to reconstruct the ALP parameters after the observation of a gamma-ray signal from a Galactic SN explosion. The results of this analysis are discussed in Sec. IV. Finally, in Sec. V we summarize and conclude.

## II. ALP-INDUCED SUPERNOVA GAMMA-RAY BURST

### A. Core-collapse supernova ALP production

ALPs are expected to be abundantly produced in CC SNe. In a minimal model we consider only their interaction with photons characterized by the Lagrangian term [16],

$$\mathcal{L}_{a\gamma} = -\frac{1}{4} g_{a\gamma} F_{\mu\nu} \tilde{F}^{\mu\nu} a = g_{a\gamma} \mathbf{E} \cdot \mathbf{B} a, \tag{1}$$

with $g_{a\gamma}$ the ALP-photon coupling, $F_{\mu\nu}$ the electromagnetic field strength tensor, $\tilde{F}^{\mu\nu}$ its dual, $a$ the ALP field, and $\mathbf{E}$, $\mathbf{B}$ are the electric and magnetic field, respectively. This interaction leads to the ALP production rate per volume in the SN core via Primakoff process [3],

$$\frac{d\dot{n}_a}{dE} = \frac{g_{a\gamma}^2 \xi^2 T^3 E^2}{8\pi^3 (e^{E/T} - 1)} \left[ \left( 1 + \frac{\xi^2 T^2}{E^2} \right) \ln \left( 1 + \frac{E^2}{\xi^2 T^2} \right) - 1 \right]. \tag{2}$$

Here, $E$ is the photon energy measured by a local observer at the emission radius, $T$ the temperature and $\xi^2 = \kappa^2/4T^2$ with $\kappa$ the inverse Debye screening length, describing the finite range of the electric field surrounding charged particles in the plasma. The total ALP production rate per unit energy is obtained integrating Eq. (2) over the SN volume.

In the limit $m_a \ll T$, the ALP spectrum is reproduced with excellent precision by the analytical expression [3,15]

$$\frac{dN_{\rm a}}{dE} = C \left( \frac{g_{a\gamma}}{10^{-12}\,\mathrm{GeV}^{-1}} \right)^2 \left( \frac{E}{E_0} \right)^{\beta} \exp\left( -\frac{(\beta+1)E}{E_0} \right), \tag{3}$$

where the values of the parameters $C$, $E_0$, and $\beta$ are related to the SN model. The expression above describes a *quasithermal* spectrum, with average energy $\langle E \rangle = E_0$ and index $\beta$ (in particular, $\beta = 2$ corresponds to a perfectly thermal spectrum of ultrarelativistic particles).

Following Ref. [15], it is possible to extract the dependence of the spectral coefficients $C$, $E_0$, and $\beta$ on the SN progenitor mass for successful CC SNe,

$$\begin{aligned} \frac{C(M)}{10^{48}\ \mathrm{MeV}^{-1}} &= (1.73 \pm 0.172) \frac{M}{M_\odot} - 9.74 \pm 2.92, \\ \frac{E_0(M)}{\mathrm{MeV}} &= (1.77 \pm 0.156) \frac{M}{M_\odot} + 59.3 \pm 2.65, \\ \beta(M) &= (-0.0254 \pm 0.00587) \frac{M}{M_\odot} + 2.94 \pm 0.0997. \end{aligned} \tag{4}$$

For our numerical analysis, we will refer to a SN model with an $11.2 M_\odot$ progenitor mass obtained using a 1D spherically symmetric and general relativistic hydrodynamics model, based on the `AGILE BOLTZTRAN` code [17,18]. In this case, an example of the time-integrated spectrum is shown in Fig. 1, with values of the spectral coefficients taken from Table I in Ref. [15].

Here, we are interested in studying the ALP detectability prospects, focusing on very weakly interacting ALPs, with $g_{a\gamma} \lesssim 10^{-11}$ GeV$^{-1}$. In this regime, ALPs have a very long mean free path even in the very dense SN core, and can escape freely. Yet, even such a tiny ALP-photon coupling may trigger a significant ALP conversion into photons in the Galactic magnetic field, as we will show in the next section.

In principle, another possible ALP production mechanism in a SN would be the conversion of thermal photons into ALPs in the intense magnetic field inside a SN core, $B \gtrsim \mathcal{O}(10^9$ G) [19–22] (see also Refs. [23,24] for studies of ALP-photon conversions in other astrophysical environments, such as the Sun and white dwarfs). However, it can be shown that the light ALP production is unaffected by the possible ALP-photon conversions inside the SN core. Indeed, the photon mean-free-path in this environment is extremely short ($\sim 10^{-8}$ cm) to allow for efficient conversions, that would take place on a length-scale $\sim \mathcal{O}(10^9$ cm) for $B \sim 10^9$ G and $g_{a\gamma} \sim 10^{-12}$ GeV$^{-1}$. On the other hand,

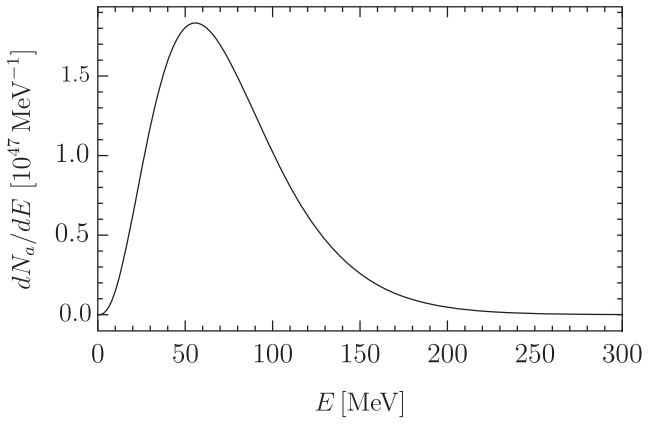


FIG. 1. Time-integrated SN ALP spectrum for $g_{a\gamma} = 10^{-12}$ GeV$^{-1}$ and $C = 7.09 \times 10^{48}$ MeV$^{-1}$, $E_0 = 75.70$ MeV and $\beta = 2.80$ [15].

ALP-photon conversions in a SN core would be relevant for MeV-scale ALPs, which are resonantly produced by the conversion of photons with plasma frequency matching the ALP mass (for transverse photon modes) or energy (for longitudinal photon modes). This process is efficient only in very energetic subclasses of SNe hosting a ultra-high magnetic fields $B \gtrsim 10^{14}$ G [25]. Regarding the standard background, the role of strong magnetic fields in the gamma-ray burst (GRB) generation is still under debate but we expect that temporal and spectral information can disentangle it from new physics.

### B. Conversion probabilities

The complex structure of the Galactic magnetic field makes the propagation of ALPs in the Milky Way a truly three-dimensional problem (see, e.g., [26]). In this work, we closely follow the technique described in Ref. [27] (to which we address the reader for more details) to solve the beam propagation equation along a Galactic line of sight.

To gain some physical intuition, however, it is also useful to study approximate analytical solutions. The problem simplifies significantly if the magnetic field **B** is homogeneous. In this case, the ALP-photon conversion probability is given by [16]

$$P_{a\gamma} = (\Delta_{a\gamma} L)^2 \frac{\sin^2(\Delta_{\rm osc} L/2)}{(\Delta_{\rm osc} L/2)^2}, \tag{5}$$

where $L$ is the path length, and the oscillation wave number is [16]

$$\Delta_{\rm osc} \equiv [(\Delta_a - \Delta_{\rm pl})^2 + 4\Delta_{a\gamma}^2]^{1/2}, \tag{6}$$

where $\Delta_a = -m_a^2/2E$, $\Delta_{\rm pl} = -\omega_{\rm pl}^2/2E$ and $\Delta_{a\gamma} = g_{a\gamma} B_T/2$, being $B_T$ the magnetic field component transverse to the photon propagation, $E$ the ALP/photon energy, and $\omega_{\rm pl}$ the plasma frequency. For benchmark values relevant for the SN ALP propagation in the Milky Way the oscillation parameters are

$$\Delta_{a\gamma} \simeq 1.5 \times 10^{-3} \left(\frac{g_{a\gamma}}{10^{-12}\ \text{GeV}^{-1}}\right)\left(\frac{B_T}{10^{-6}\ \text{G}}\right)\ \text{kpc}^{-1},$$
$$\Delta_a \simeq -7.8 \times 10^{-5} \left(\frac{m_a}{10^{-11}\ \text{eV}}\right)^2 \left(\frac{E}{100\ \text{MeV}}\right)^{-1}\ \text{kpc}^{-1},$$
$$\Delta_{\rm pl} \simeq -7.8 \times 10^{-7} \left(\frac{\omega_{\rm pl}}{10^{-12}\ \text{eV}}\right)^2 \left(\frac{E}{100\ \text{MeV}}\right)^{-1}\ \text{kpc}^{-1}.$$

Therefore, for the typical conditions that we consider, $\Delta_{\rm pl} \ll \Delta_a, \Delta_{a\gamma}$ and thus it is always negligible in our analysis. The conversion probability in Eq. (5) can be further simplified in the two opposite limits of $\Delta_a \gg \Delta_{a\gamma}$ and $\Delta_a \ll \Delta_{a\gamma}$. In particular, for $\Delta_a \ll \Delta_{a\gamma}$, corresponding to

$$m_a \ll m_a^l = 0.044\ \text{neV} \left(\frac{g_{a\gamma}}{10^{-12}\ \text{GeV}^{-1}}\right)^{1/2} \times \left(\frac{B}{10^{-6}\ \text{G}}\right)^{1/2} \left(\frac{E}{100\ \text{MeV}}\right)^{1/2}, \tag{7}$$

the conversion probability becomes energy independent. Furthermore, for typical Galactic baselines $L \lesssim 10$ kpc and in the conditions of interest for our problem, we can assume $\Delta_{a\gamma} L \ll 1$, which reduces the oscillation probability to

$$P_{a\gamma} \simeq (\Delta_{a\gamma} L)^2. \tag{8}$$

In the opposite limit of $m_a \gg m_a^l$, $\Delta_{\rm osc} \approx \Delta_a$ and

$$P_{a\gamma} \simeq 4 \left(\frac{\Delta_{a\gamma}}{\Delta_a}\right)^2 \sin^2(\Delta_a L/2), \tag{9}$$

which exhibits an energy-dependent oscillatory behavior. However, when $\Delta_a L \ll 1$, i.e.

$$m_a \ll m_a^h = 0.36\ \text{neV} \left(\frac{E}{100\,\text{MeV}}\right)^{1/2} \left(\frac{L}{10\,\text{kpc}}\right)^{-1/2}, \tag{10}$$

one can expand $\sin^2(\Delta_a L/2) \sim \Delta_a^2 L^2/4$ and the energy-independent probability in Eq. (8) is recovered. For the conditions considered in this paper, $m_a^h \gg m_a^l$, therefore we dub $m_a^c \equiv m_a^h$ as the critical mass below which the probability is energy independent. Above this threshold, for $m_a \gtrsim m_a^c$, the probability scales as $P_{a\gamma} \sim \Delta_a^{-2}$, modulated by fast oscillations that are typically smeared out by the detector finite energy resolution, see also discussion below.

### C. Models of Galactic magnetic field

Realistic estimates of the ALP-photon conversion probability in the Galaxy rely on the specific morphology of the Milky Way magnetic field. As we shall see, the uncertainties related to the modeling of the Galactic magnetic field contribute significantly to the total uncertainty in our results. In this work we consider three different state-of-the-art magnetic field models (neglecting their turbulent components [28]), often taken as benchmark in the context of ALP conversions:

(i) "JF": Jansson and Farrar model [29], which includes a disk field and an extended halo field with an out-of-plane component, based on the WMAP7 Galactic Synchrotron Emission map [30] and extragalactic Faraday rotation measurements.

(ii) "JFnew": Jansson and Farrar model [29] with the updated parameters given in Table C.2 of [31] ("Jansson12c" ordered fields), to match the polarized synchrotron and dust emission measured by the Planck satellite [32–34]. In this work, we use "JFnew" as our benchmark model.

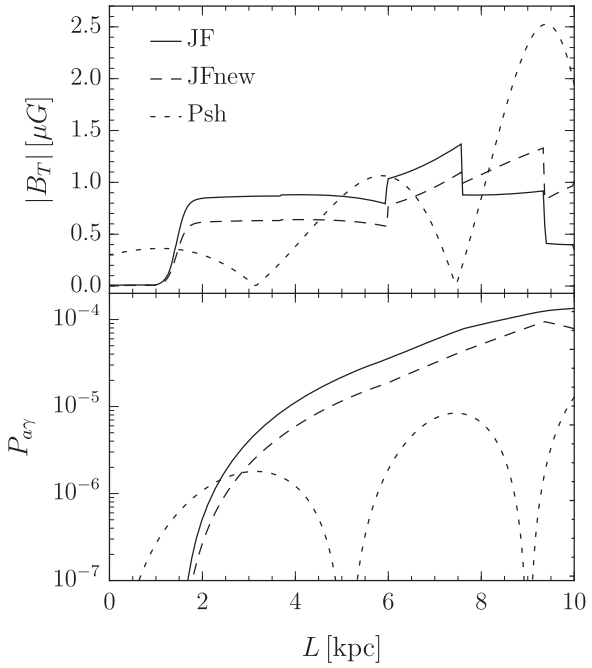


FIG. 2. Amplitude of the transverse magnetic field $B_T$ (upper panel) and probability for $m_a \lesssim \mathcal{O}(0.1)$ neV, $E = 100$ MeV and $g_{a\gamma} = 10^{-12}$ GeV$^{-1}$ (lower panel) as a function of the distance from the source in the direction $(\ell, b) = (199.79°, -8.96°)$ for "JF" (black), "JFnew" (dashed black) and "Psh" (dotted black) models. Note that the source is placed in $L = 0$ and the Earth is in $L = 10$ kpc.

(iii) "Psh": Pshirkov model [35], presenting a symmetric (with respect to the Galactic plane) spiral disk and antisymmetric halo field, based on rotational measures of extragalactic radio sources [36].

In the upper panel of Fig. 2, we compare the transverse magnetic field for the different magnetic models listed above in direction $(\ell, b) = (199.79°, -8.96°)$,[2] over a distance of 10 kpc from the Earth, i.e. the source is placed in $L = 0$ and the Earth is in $L = 10$ kpc. For this specific line of sight, the "JF" (solid line) and "JFnew" (dashed line) models predict a transverse magnetic field with a similar shape, where the prediction of "JFnew" is larger than "JF" for $L > 8$ kpc. On the other hand, the "Psh" model (dotted line) leads to a different morphology, featuring a smaller average transverse magnetic field despite the higher values for $L \gtrsim 9$ kpc and $L \lesssim 1.5$ kpc compared to the previous models. These different behaviors reflect on the profile of the conversion probability as a function of the distance from the source, as shown in the lower panel of Fig. 2 for $m_a \lesssim \mathcal{O}(0.1)$ neV, $E = 100$ MeV and $g_{a\gamma} = 10^{-12}$ GeV$^{-1}$. The value of the probability relevant for observations is the one for $L = 10$ kpc, where the Earth is placed, and it is evident that "JF" and "JFnew" lead to conversion probabilities of $\mathcal{O}(10^{-4})$, one order of magnitude larger than the one obtained with the "Psh" model.

It is useful to compare the exact conversion probability obtained from a numerical integration of the equations of motion with the analytical expression in Eq. (5), assuming a uniform magnetic field, obtained averaging the real one over the line of sight [compare with Eq. (A23) in Ref. [37] ], i.e.

$$\langle B_T \rangle^2 = \frac{1}{L^2}\left[\left|\int_0^L dz B_x(z)\right|^2 + \left|\int_0^L dz B_y(z)\right|^2\right], \qquad (11)$$

assuming ALPs propagating along $z$ over a distance $L$, while $B_x$ and $B_y$ are taken from the different magnetic field models. This approximation is useful to analyze how the signal is affected by the ALPs mass. In Fig. 3 we show the conversion probability $P_{a\gamma}$ as a function of the ALP mass $m_a$ evaluated by the approximate expression in Eq. (5) (red line) and compared with the exact result (black line), for $g_{a\gamma} = 10^{-12}$ GeV$^{-1}$, $E = 100$ MeV and $L = 10$ kpc.

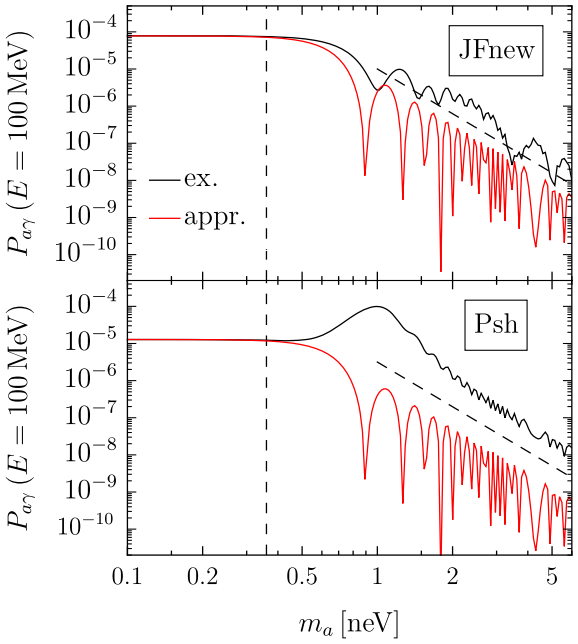


FIG. 3. ALP-photon conversion probability $P_{a\gamma}$ for an ALP energy $E = 100$ MeV and ALP-photon coupling $g_{a\gamma} = 10^{-12}$ GeV$^{-1}$ as a function of the ALPs mass $m_a$, numerically evaluated for two models of the Galactic magnetic field (black curves) and using the analytical approximation for the average $B$-field (red curves). In the upper panel the "JFnew" model is used, while in the lower panel we refer to the "Psh" model. The vertical dashed black line represents transition region around the critical mass $m_a^c \simeq 0.36$ neV at which $\Delta_a L = 1$. The oblique dashed line indicates the behavior $m_a^{-4}$, followed by the oscillation probabilities at masses larger than the critical mass, and it is displayed only to guide the eye (see main text for more details).

[2]The coordinates used here correspond to direction of Betelgeuse; however, this is just to provide a concrete example. Our analysis is intended to be general and not related to a specific star.

In the approximate formula we use $\langle B_T \rangle = 0.58$ μG for "JFnew" (upper panel), leading to $P_{a\gamma} = 7.8 \times 10^{-5}$ in the low-mass limit, $m_a \lesssim 0.36$ neV [see Eq. (10)], indicated with the vertical dashed line, and $\langle B_T \rangle = 0.24$ μG for "Psh" (lower panel), resulting in $P_{a\gamma} = 1.3 \times 10^{-5}$ in the same limit. For $m_a \lesssim 0.36$ neV, the approximate and exact results are in agreement since the ALP oscillation length $l_{\rm osc} = 2\pi/\Delta_{\rm osc} \approx 3.5 \times 10^3$ kpc for the chosen input values is much larger than the dimension of the Galaxy. Thus, the conversion probability mainly depends on $\langle B_T \rangle$. For larger masses, the oscillation length becomes smaller (e.g., $l_{\rm osc} \sim 1$ kpc at $m_a = 3$ neV), making the oscillations sensitive to the detailed structures of the $B$-field. In this latter case, the conversion probabilities evaluated in the exact models are larger than the constant magnetic field approximation. This behavior can be explained using the perturbative approach discussed in Ref. [38]. In essence, the conversion probability is proportional to the power spectrum of the magnetic field along the line of sight, which is increased by the presence of inhomogeneities. Hence, neglecting them in the constant field approximation reduces the oscillation probability. Nevertheless, in agreement with our previous discussion, both results exhibit a $m_a^{-4}$ behavior, as shown by the dashed line, added in Fig. 3 to guide the eye.

### D. Observable gamma-ray spectrum

The gamma-ray flux in units of $\mathrm{MeV}^{-1}\,\mathrm{cm}^{-2}$ that reaches the Earth is given by

$$\frac{d\phi_\gamma}{dE} = \frac{1}{4\pi L^2}\frac{dN_{\rm a}}{dE} P_{a\gamma}(E). \tag{12}$$

The shape of the observed photon spectrum is determined by the finite detector energy resolution, producing the following smearing

$$\frac{d\phi_{\gamma,\rm obs}}{dE_\gamma} = \int_{-\infty}^{+\infty} \eta(E, E_\gamma)\frac{d\phi_\gamma}{dE}(E)dE, \tag{13}$$

where $E$ is the true photon energy, $E_\gamma$ is the detected one, and $\eta(E, E_\gamma)$ is the detector dispersion matrix.

To illustrate this point, in Fig. 4 we show the observable gamma-ray signal induced by SN ALPs (right panels).

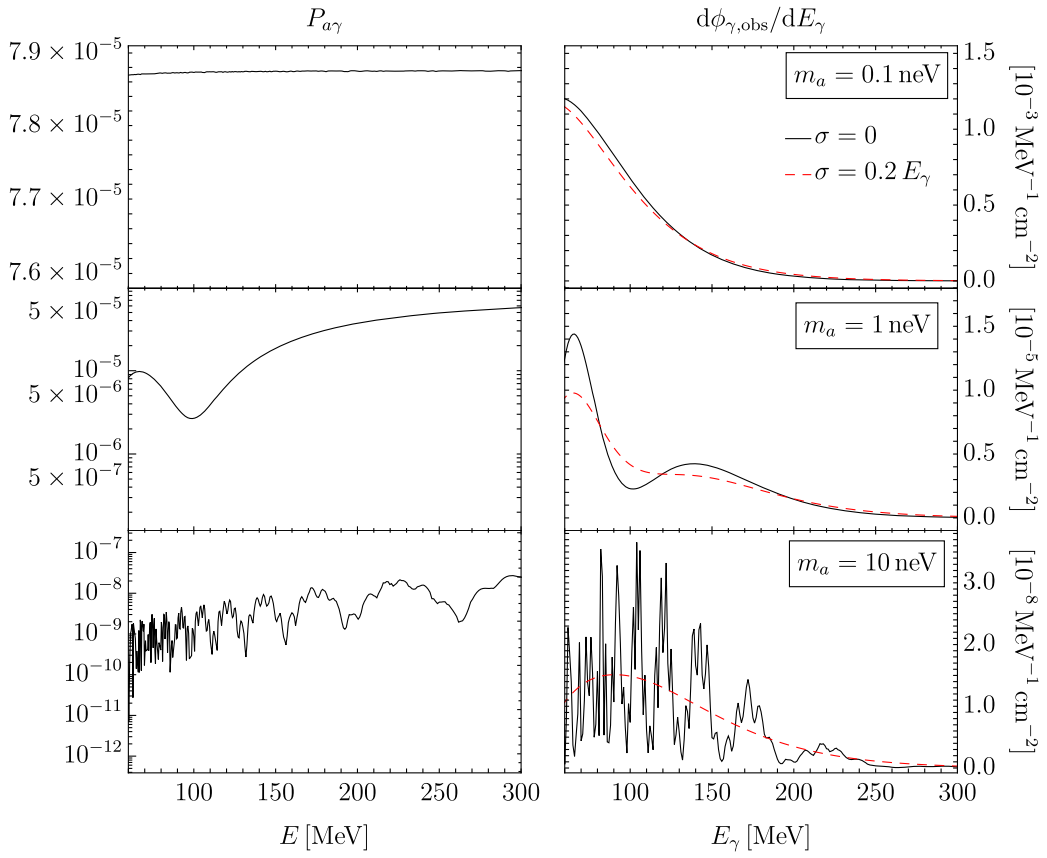


FIG. 4. Left panels: Conversion probability $P_{a\gamma}$ as a function of the ALP energy $E$. Right panels: Observable photon spectra at the detector. The ALP parameters are $g_{a\gamma} = 10^{-12}$ GeV$^{-1}$ and $m_{\rm a} = 0.1$ neV (upper panel), $m_{\rm a} = 1$ neV (middle panel) or $m_{\rm a} = 10$ neV (lower panel). We consider the cases of perfect energy resolution ($\sigma = 0$, black solid lines) and Gaussian energy resolution with $\sigma(E_\gamma) = 0.2E_\gamma$ (dashed red lines).

The ALP parameters are $g_{a\gamma} = 10^{-12}$ GeV$^{-1}$ and $m_a =$ 0.1 neV (upper panel), $m_a = 1$ neV (middle panel) or $m_a = 10$ neV (lower panel). We consider the cases of perfect energy resolution ($\sigma = 0$, black solid line) and Gaussian energy resolution with $\sigma(E_\gamma) = 0.2E_\gamma$ (dashed red line). The latter is a good approximation for the LAT energy resolution for energies larger than 60 MeV, thus we assume a threshold for observation $E_{\rm th} = 60$ MeV. The SN is assumed to be at a distance of $L = 10$ kpc, in the same direction, $(\ell, b) = (199.79°, -8.96°)$, specified above, and the magnetic field model is "JFnew". In the left panels of Fig. 4, we display the relevant conversions probabilities $P_{a\gamma}$ as a function of the ALP energy $E$.

As shown in the upper left panel of Fig. 4, for $m_a = 0.1$ neV the conversion probability is constant, and thus the effect of the finite-energy resolution does not affect the observed gamma-ray signal, which keeps the same shape of the original ALP spectrum (see Fig. 1). Instead, for the other two cases, $P_{a\gamma}$ is energy dependent. This would imprint peculiar wiggles in the photon spectrum, which are, however, washed out by the finite-energy resolution of the detector (dashed red line in right panels), especially in the $m_a = 10$ neV case (lower panel). Depending on the resolution function, there may be an intermediate case, e.g. for $m_a = 1$ neV (middle panel), in which also after the energy smearing caused by the finite resolution there is some peculiar energy-dependent modulation of the spectrum. However, this is expected to happen only in a very narrow range of ALP masses. The discussion above suggests that there are three different ALP mass ranges with peculiar properties of the expected signal. In absence of wiggles, the observed photon flux in MeV$^{-1}$ cm$^{-2}$ integrated over the SN explosion time can be very well-described by the function

$$\frac{d\phi_{\gamma,\rm obs}}{dE_\gamma} = C_{\rm obs}\left(\frac{E_\gamma}{\epsilon_0}\right)^\alpha \exp\left(-\frac{(\alpha+1)E_\gamma}{\epsilon_0}\right), \quad (14)$$

which resembles the form of the ALP spectrum in Eq. (3), but with different parameters, depending on the considered ALP mass range:

(1) $m_a \ll m_a^c$. *Energy-independent conversions*. The gamma-ray spectrum has the same shape of the initial ALP spectrum as in Eq. (3). Thus, comparing it with the original ALP spectrum in Eq. (3), the spectral index is $\alpha \simeq \beta$ and the average energy of the observed photon spectrum is $\epsilon_0 = \langle E_\gamma \rangle \simeq E_0$.

(2) $m_a \gg m_a^c$. *Averaged conversions* with $P_{a\gamma} \sim 2\Delta_{a\gamma}^2/\Delta_a^2$. The wiggles in the gamma-ray spectrum induced by ALP conversion are so dense that they are completely smoothed out by the effect of the detector. In this case, $P_{a\gamma} \propto E_\gamma^2$. Thus, the photon spectrum acquires an additional dependence on the energy. Explicitly, we find $\alpha = \beta + 2$ and $\epsilon_0 = \langle E_\gamma \rangle \simeq \frac{\beta+3}{\beta+1} E_0$.

(3) $m_a \approx m_a^c$. *Intermediate regime*. This is a narrow range where the signal wiggles are not completely washed out by the detector resolution, so we do not expect a smooth functional form in this case and the fit in Eq. (14) does not apply.

In Fig. 5 we show the results of fitting the three observed spectra from Fig. 4 with Eq. (14). The $m_a = 0.1$ neV (upper left panel) is representative of case 1 in which $P_{a\gamma}$ is energy independent, therefore the best-fit parameters $\alpha = 2.0$ and $\epsilon_0 = 73.2$ MeV are close to the average energy $E_0$ and spectral index $\beta$ of the *primary* ALP flux. From the plot of the residual it is apparent that the fit worsens in the high-energy tail of the spectrum, at $E_\gamma \gtrsim 150$ MeV, where the discrepancy between the observed flux and the fitted expression is more than 20%.

The case of $m_a = 1$ neV (upper right panel) corresponds to case 3. Here, due to the energy threshold of the detector, the peak of the energy spectrum is not visible and we can see only the tails. Thus, the fit in Eq. (14) does not work and we can try to fit the observed spectrum with an exponential function $d\phi_{\gamma,\rm obs}/dE_\gamma \propto \exp(-k_1 E_\gamma)$, with $k_1$ fitting parameter. In this case, the fitting function presents deviations and a remaining energy-dependent modulation of the order of 20% due to remnant of the oscillatory behavior of the probability after the smearing due to the resolution.

Finally, the plot with $m_a = 10$ neV (lower panel) corresponds to case 2. We see that in the energy range $E_\gamma \in [60; 200]$ MeV the deviations of the fitting function with respect to the numerical spectrum are less than 10%, smaller than the ultralight case due to the larger average energy of the observed photon spectrum.

We see that the values of the fitting parameters $\alpha = 3.7$ and $\epsilon_0 = 116.9$ MeV are significantly larger than the ones expected from the original ALP spectrum of Eq. (3). This feature can be used as a way to distinguish case 3 from case 1. Specifically, a value of $\alpha \sim 2$ indicates $m_a \ll m_a^c$, while a larger value, $\alpha \sim 4$, can be considered as evidence of $m_a \gg m_a^c$.

## III. RECONSTRUCTION OF THE SIGNAL

The ALP burst expected from a future Galactic CC SN originates a gamma-ray transient, which falls in the sensitivity range of Fermi-LAT. The LAT enables the detection and re-construction of primary gamma rays of energies from 20 MeV to more than 300 GeV via pair production in its tracker and calorimeter. Per instant of time, it covers a wide field of view of ~2.4 sr [39] making it ideal for the study of transient events. In what follows, we assess the potential of the LAT to reconstruct ALP parameters if it detects a gamma-ray burst coming from a Galactic SN explosion during its remaining lifetime. To this end, we rely on simulated data of Fermi-LAT based on the spectra of signal and background components. The simulations are performed with the Fermi Science Tools

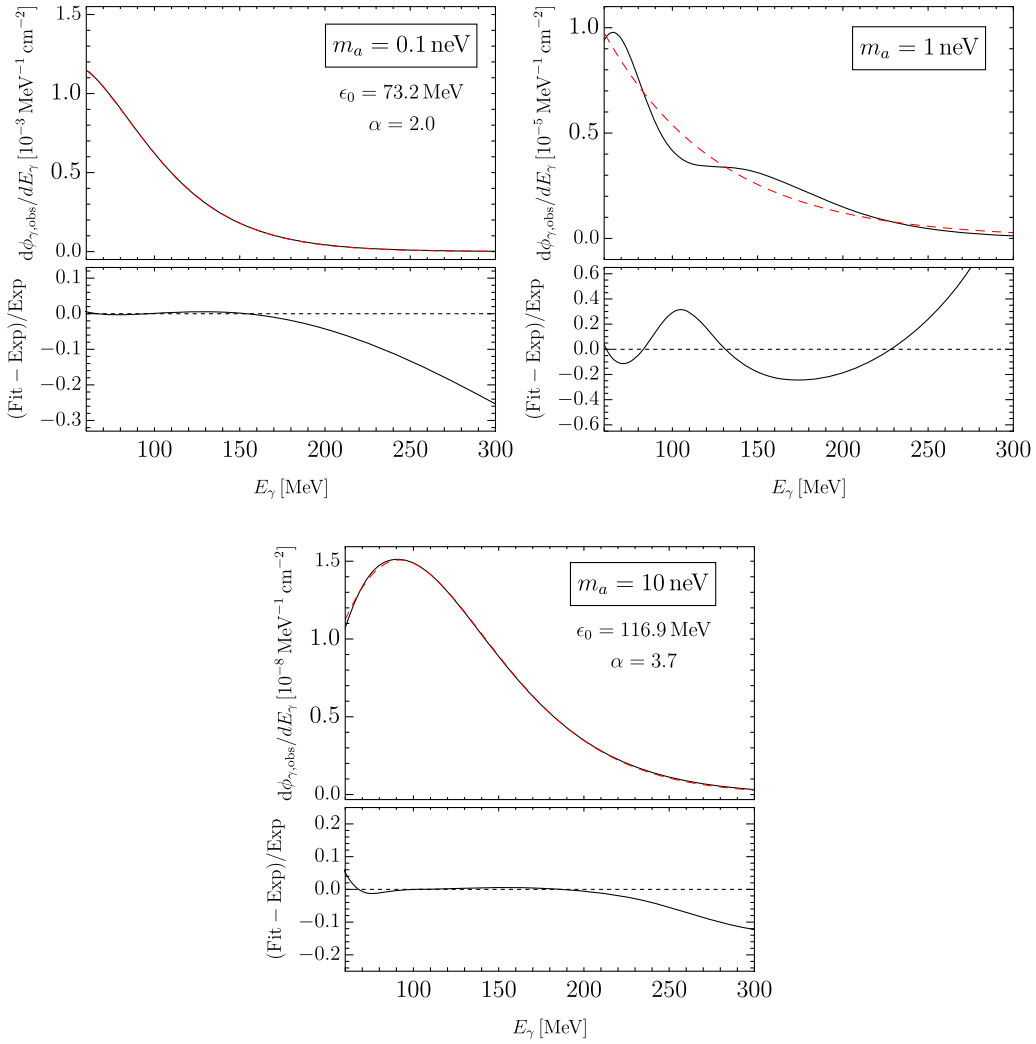


FIG. 5. Photon spectra expected to be observed (black lines) and their fit (dashed red lines) given by Eq. (14) for $g_{a\gamma} = 10^{-12}$ GeV$^{-1}$ and $m_a = 0.1$ neV (upper left), $m_a = 1$ neV (upper right) or $m_a = 10$ neV (lower panel). In each panel, we show also the residuals, defined as the relative difference between the fitted spectrum (Fit) and the expected one (Exp).

(version 2.0.8).[3] Our sensitivity estimate and simulation assume that the SN transient event will be in the LAT field of view for the entire burst duration. We therefore do not account for the probability of the LAT to see the SN, and we refer to Ref. [13] for more details.

### A. Gamma-ray burst simulation

We simulate gamma-ray bursts from a Galactic CC SN given by the flux in Eq. (12). To this end, we will use the fit of the ALP flux obtained from the numerical SN simulation of an $11.2M_\odot$ stellar progenitor at a distance of $L = 10$ kpc in the direction $(\ell, b) = (199.79°, -8.96°)$ [see footnote 2]. We assume that the gamma-ray burst lasts for $t_{\mathrm{obs}} = 18$ s.

These burst input data are converted into individual gamma-ray events with the Fermi Science Tools routine `gtobssim` based on the `FileSpectrum` class.[4] All simulations rely on the `P8R3_TRANSIENT020_V3` event class (Pass8, release 3) and `FRONT+BACK` event types. We apply further cuts on the selected sample of photons via the requirement of an event zenith angle $< 80°$, which reduces the contamination of this sample by Earth limb photons, and the additional quality cuts `DATA_QUAL>0 && LAT_CONFIG==1`. We simulate the events in the energy range from 60 MeV to 600 MeV. We do not extend our analysis below 60 MeV since the Fermi-LAT effective area is rapidly decreasing at lower energies. Moreover, we

[3] https://fermi.gsfc.nasa.gov/ssc/data/analysis/software/.

[4] See also fermi.gsfc.nasa.gov for a detailed description of the routine's functionalities.

consider events arriving from a cone with a radius of 10° around the position of the SN explosion. Since we cannot simulate Fermi-LAT data in the future, we resort to a typical time interval of duration $t_{\rm obs}$ in the past observation history of the instrument. For our purposes, such a typical time is characterized by an exposure in the direction $(\ell, b) = (199.79°, -8.96°)$ close to the median value obtained from considering all available time intervals of length $t_{\rm obs}$. In addition, the explosion is such that it falls completely within a good time interval (GTI) of the LAT. These criteria are fulfilled for $T_{\rm ON} = 510,\ 160,\ 000$ MET,[5] which we adopt as the onset time of the CC SN.

### B. Estimating the sensitivity of the LAT to $g_{a\gamma}$

One crucial aspect of the ALP burst analysis is the overall sensitivity of the LAT to detect the ALP-induced gamma-ray burst from a CC SN, i.e. the minimal coupling the LAT will be sensitive to. Here, we detail the approach designed to derive the sensitivity for the hypothetical case of an $11.2M_\odot$ CC SN in the direction $(\ell, b) = (199.79°, -8.96°)$.

A suitable statistical framework can be developed from the study presented in [13], where the authors analyzed the sensitivity of Fermi-LAT to the ALP-flux from CC SN events in the Milky Way and M31. Their sensitivity estimates allowed the projection of upper limits on the ALP parameter space for events occurring within a GTI of the LAT. The approach comprises the following steps:

(1) Select a single day of LAT data when a CC SN is going to occur.
(2) Determine all GTIs of this day in the direction of the CC SN (including additional data quality cuts such as zenith angle, Earth limb, etc.).
(3) Simulate a CC SN in one of these GTIs.
(4) Calculate the LAT exposure for each of these GTIs.
(5) Sum the detected events in each GTI except for the one where the CC SN has happened. These are considered "OFF" counts $N_{\rm OFF,i}$ and used to create an estimator for the expected background counts $\hat{b}$ in the "ON" GTI (where the CC SN has exploded). The value of $\hat{b}$ follows from maximizing the Poisson likelihood function

$$\mathcal{L} = \prod_i \frac{(\varepsilon_i b)^{N_{\rm OFF,i}}}{(N_{\rm OFF,i})!} e^{-\varepsilon_i b}, \tag{15}$$

with respect to the background counts $b$, where $\varepsilon_i = \mathcal{E}_{\rm OFF,i}/\mathcal{E}_{\rm ON}$ is the ratio of exposures in the respective OFF region and ON region (to rescale the background estimator to the OFF exposure since it is going to be determined for the ON-region). It follows that

$$\hat{b} = \frac{\sum_i N_{\rm OFF,i}}{\sum_i \frac{\mathcal{E}_{{\rm OFF},i}}{\mathcal{E}_{\rm ON}}}. \tag{16}$$

(6) Upper limits follow from the ON Poisson likelihood function including the expected average signal counts $s$ derived from the assumed model:

$$\mathcal{L} = \frac{(s+\hat{b})^{N_{\rm ON}}}{(N_{\rm ON})!} e^{-(s+\hat{b})}. \tag{17}$$

In their case and since there are no true ON counts, they assume a so-called Asimov data set by setting $N_{\rm ON} = \hat{b}$ (counts must be integers; hence, they take the next integer greater than $\hat{b}$).
(7) Upper limits at a certain confidence level are directly constructed from the containment belts following Ref. [40], which provided a scheme that also works when background and signal are small.

Instead of the total photon counts of a burst, we use a different observable related to the time series of the burst; the time delay among consecutive photons, $\delta\tau_N$, where the index $N$ denotes the size of the group of photons for which the time delay is measured. For example, $\delta\tau_5$ means that we consider the difference in arrival time of one selected photon and the fifth photon detected after that. In a real burst of a few seconds (either long or short gamma-ray burst), this time delay should be quite small among the photons associated with the event, while there is no such correlation among photons produced by nontransient events. Considering $\delta\tau_N$ or the total number of counts is rather equivalent for the case of Galactic gamma-ray bursts since the onset of the transient can be well-localized with the help of multimessenger signals such as neutrinos [41]. The advantage of $\delta\tau_N$ is mainly in the context of searches for extragalactic SN explosions (or other transients) where no independent measure of their onset time exists. The information in the time series helps distinguish between upwards fluctuations of photon counts and a genuine transient event characterized by correlated photon arrival times. In this work, we examine $\delta\tau_3$, $\delta\tau_4$ and $\delta\tau_5$.

We have modified the approach to consider the time delay discussed above as the ALP observable for determining the LAT sensitivity. We employ the following rationale:

(1) We use a time interval $\Delta t = 30$ s to derive the time series. In the case of a Galactic CC SN, we will have the neutrino signal as the trigger, which allows us to precisely determine the onset of the burst. This choice of $\Delta t$ ensures that the burst signal is well-contained in the ON bin.
(2) We simulate a CC SN in the selected ON region containing $T_{\rm ON}$ and consider the remaining time

[5]Mission elapsed time (MET) is the number of seconds since the reference time of January 1, 2001, at 0h:0m:0s in the Coordinated Universal Time (UTC) system.

intervals as OFF regions. We use real data to determine the background.

(3) In the ON region, we simulate the CC SN event multiple times and obtain time series histograms, saving the number of entries in the first time bins (time delay of less than a second/five seconds for $\delta\tau_3/\delta\tau_4/\delta\tau_5$). We derive the mean expected numbers and repeat for various coupling constant values.

(4) We calculate the same histograms and extract the entries in the first bins for each OFF region. We obtain the LAT exposure in the ON and all OFF regions using the Fermi Science Tools routines `gtselect`, `gtmktime`, `gtbin` (LC—light curve—with weekly binning), and `gtexposure`. We derive the estimator for the background counts for each histogram, respectively.

(5) We construct containment belts with the method described in [40] and derive upper limits for each individual histogram quantity based on the Asimov approach.

(6) The final upper limit is the minimal value among the three computed upper limits.

### C. Reconstructing ALP parameters from time-integrated burst spectra

We employ the Fermi-LAT data analysis framework of [8] to extract model parameters related to ALPs causing the detection of gamma-ray emission from a future nearby SN. Briefly, we fit the model for the time-integrated gamma-ray flux in Eq. (14) to mock observations in order to reconstruct the observed parameters $C_{\rm obs}$, $\alpha$ and $\epsilon_0$ using the generalized Poisson likelihood function

$$\mathcal{L}(\boldsymbol{\mu}=\boldsymbol{S}+\boldsymbol{B}+\boldsymbol{\delta B}|\boldsymbol{n}) = \prod_{i=1}^{N_E} \frac{(S_i+B_i+\delta B_i)^{n_i}}{(n_i)!} e^{-(S_i+B_i+\delta B_i)} \times \exp\left[-\frac{1}{2}\sum_{j,k=1}^{N_E} \delta B_j (K^{-1})_{jk} \delta B_k\right]. \tag{18}$$

The likelihood function involves the ALP-induced gamma-ray emission $\boldsymbol{S}$, expected background $\boldsymbol{B}$, fluctuations due to finite energy resolution $\boldsymbol{\delta B}$, and observed mock data $\boldsymbol{n}$ split into $N_E$ energy bins. Background, signal and mock data are simulated and analyzed at the photon counts level. The covariance matrix $K_{ij}$ parametrizes the correlation between spectral fluctuations $\boldsymbol{\delta B}$ (associated with both the signal and background), with values obtained from extracting the LAT energy dispersion with respect to the chosen event class using the Fermi Science Tools.

The posterior distributions of the model parameters are computed in a Bayesian approach, profiling over nuisance parameters $\boldsymbol{\delta B}$ in a maximum likelihood fit with `iminuit` [42] and employing the profiled log-likelihood function $-2\ln\mathcal{L}_{\rm prof}$ to derive the (marginal) posterior distributions using `MultiNest` [43] (specifying 1000 live points and an evidence tolerance of 0.2). For a detailed description of the method, please refer to our previous publication [8].

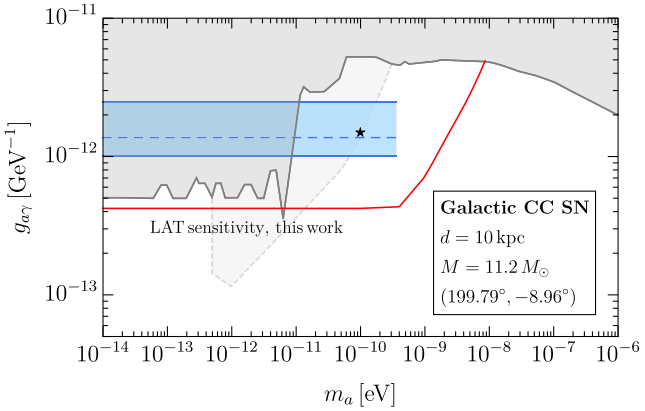


FIG. 6. Comparison of the projected 95% confidence level Fermi-LAT sensitivity to $g_{a\gamma}$ (displayed in red) for an ALP-induced gamma-ray burst from a CC SN with the benchmark characteristics shown in the box and detailed in Sec. III A, alongside the current astrophysical constraints [13,44–47], shown in gray (see Ref. [48] and references therein for more details). The black star shows the benchmark ALP parameters $(m_a, g_{a\gamma}) = (0.1\ \text{neV}, 1.5\times10^{-12}\ \text{GeV}^{-1})$, discussed in Sec. IV B. The dashed blue line and the light blue band represent the reconstructed coupling and the $1\sigma$ error interval, respectively. The light gray region delimited by the dashed line is the axion star explosion limit, obtained assuming ALP dark matter [49].

In what follows, we will explore the ALP parameter reconstruction potential of Fermi-LAT for couplings $g_{a\gamma} \gtrsim 10^{-12}\ \text{GeV}^{-1}$, well above the detection threshold for ALP-induced bursts given $m_a \lesssim \mathcal{O}(0.1)$ neV (cf. Fig. 6). Hence, we make the simplifying assumption that $\boldsymbol{B} \equiv 0$. This approximation is justified by the fact that in the short interval of the gamma-ray burst, i.e. 18 s, no substantial background is found. As stated in Ref. [13], the mean number of background counts over the full energy range considered here is around 1 for intervals of 20 seconds.

All simulated data does include the time-dependent features of the ALP flux according to the results of the numerical simulations. We describe here the procedure we follow to translate from the time-dependent to the time-integrated quantities. The time-dependent ALP spectrum is described by

$$\frac{dN_{\rm a}}{dEdt} = C(t)\left(\frac{g_{a\gamma}}{10^{-12}\ \text{GeV}^{-1}}\right)^2 \times \left(\frac{E}{E_0(t)}\right)^{\beta(t)} \exp\left(-\frac{(\beta(t)+1)E}{E_0(t)}\right). \tag{19}$$

We find that the dependence of the parameters $C, \beta$ and $E_0$, for the considered $11.2M_\odot$ SN model, can be very well approximated by

$$C(t) = \tilde{C}\left(\frac{t}{t_0}\right)^{0.545} e^{-0.184t/t_0},$$
$$E_0(t) = \tilde{E}_0\left(\frac{t}{t_0}\right)^{0.085} e^{-0.023t/t_0},$$
$$\beta(t) = \tilde{\beta}\left(\frac{t}{t_0}\right)^{0.048} e^{-0.005t/t_0}, \quad (20)$$

where $t_0 = 1$ s, $\tilde{C} = 6.56 \times 10^{47}\,\mathrm{MeV^{-1}\,s^{-1}}$, $\tilde{E}_0 = 75.69$ MeV and $\tilde{\beta} = 2.67$. Numerically integrating this time-dependent burst spectrum from 0 to 18 s (in accordance with the simulated gamma-ray burst duration) we obtain the time-integrated spectrum in Eq. (3), leading to the time-integrated photon flux fitted with the formula in Eq. (14), employing the energy range from 60 MeV to 600 MeV. In our gamma-ray burst simulations we vary $\tilde{C}, \tilde{\beta}$ and $\tilde{E}_0$ which—via this algorithm—directly translate to the time-integrated quantities $C_{\rm obs}$, $\alpha$ and $\epsilon_0$. In line with this procedure, we prepare a regular grid for the three parameters $\tilde{C} \in [1\!:\!20] \times 10^{47}\,\mathrm{MeV^{-1}\,s^{-1}}$, $\tilde{\beta} \in [2.5\!:\!2.9]$ and $\tilde{E}_0 \in [68\!:\!82]$ MeV entering our model $\boldsymbol{S}$ for the ALP burst spectrum in Eq. (3). We simulate the generated parameter tuples 30 times (different Poisson realizations of the same observation conditions and ALP burst parameters) with `gtobssim` and take the average to derive the signal model by interpolating the probed data points. Our input (mock) data $\boldsymbol{n}$ from which we infer the underlying ALP parameters is a single Poisson realization of a specific parameter set (see Sec. IV B).

## IV. RESULTS AND DISCUSSION

### A. Fermi-LAT sensitivity to a Galactic SN

In Fig. 6, we present the anticipated Fermi-LAT sensitivity at 95% confidence level to $g_{a\gamma}$ for an ALP-induced gamma-ray burst associated with an $11.2M_\odot$ stellar progenitor SN explosion at a distance $L = 10$ kpc. Using the method described in Sec. III B, we find that the LAT could probe currently unexplored ALP masses and couplings. From the LAT data taken in the direction $(\ell, b) = (199.79°, -8.96°)$, we estimate that the average background contribution is $\hat{b} \approx 0$ regarding all three consecutive time-delay observables. Thus, we use $N_{\rm ON} = 1$ as the background expectation in the selected "ON" GTI. From the considered dataset we can also estimate the probability of detecting a SN event in the chosen direction. About one third of the 30 s GTIs exhibit a nonzero exposure of the LAT. It is only in these time frames that a SN explosion can be detected. If we further require that the full burst duration of 18 s is encompassed by the temporal boundaries, than the most optimistic probability to capture such a SN is around 13%. However, the LAT can be oriented towards the SN direction in case of a SN alert [50], increasing the probability of a detection.

Despite extensive coverage by other astrophysical probes [48], the Fermi-LAT would explore an unprobed region of the ALP parameter space for $m_a \lesssim 10$ neV, as evident from Fig. 6, where the gray region delimited by the solid line is excluded by astrophysical arguments [13,44–47]. Hence, a future SN observation by the LAT would significantly improve the ALP parameter space coverage, as already discussed in Ref. [13]. Let us comment, however, that our sensitivity (reaching $g_{a\gamma} \simeq 4 \times 10^{-13}\,\mathrm{GeV^{-1}}$) is about a factor of two smaller than the reported sensitivity in Ref. [13], which considered a SN at the Galactic Center, and hence closer to Earth and in a region where the magnetic field is stronger. We note that this estimate is influenced by uncertainties in the Galactic magnetic field modeling, which would affect the sensitivity of a factor ∼2 at most, in excess or defect. In Fig. 6, the light gray region delimited by the dashed line is constrained by the Planck legacy measurement of the cosmic microwave background optical depth, which can be altered by the explosion of axion stars [49]. Indeed, axion star decays would inject photons into the intergalactic medium (IGM), heating it and leading to an efficient ionization of the IGM, strongly constrained by Planck data [51,52]. This constraint would supersede the Fermi-LAT sensitivity for ALP masses $5 \times 10^{-13}\,\mathrm{eV} \lesssim m_a \lesssim 10^{-11}$ eV. However, it is valid only if ALPs are dark matter, an assumption not required in this work. In addition, as further discussed in Ref. [49], this bound is largely affected by uncertainties. For instance, it could be modified by different assumptions on core-halo mass relations, still under debate [49,53–55], and possible ALP self-interactions, which are neglected to obtain the constraint in Fig. 6. For the aforementioned reasons, we neglect this constraint in the following discussion.

### B. ALP parameter reconstruction for $m_{\rm a} \lesssim m_a^c$

Here, we discuss how to reconstruct the ALP-photon coupling in the case of a detection of an ALP-induced gamma-ray burst in coincidence with a future Galactic SN explosion. We build upon the established Fermi-LAT sensitivity to constrain the spectral parameters of the gamma-ray burst when its luminosity is above the derived sensitivity threshold for ALP masses $m_a \lesssim O(0.1)$ neV, below the critical mass $m_a^c = 0.36$ neV introduced in Sec. II D. Then, we analyze the integrated spectrum of the burst according to the statistical approach outlined in Sec. III C.

Specifically, we consider $m_a = 0.1$ neV and five different coupling strengths $g_{a\gamma} \in [1, 1.5, 2, 2.5, 3] \times 10^{-12}\,\mathrm{GeV^{-1}}$ to simulate a mock observation. This allows us to comprehensively quantify the uncertainties on the reconstructed

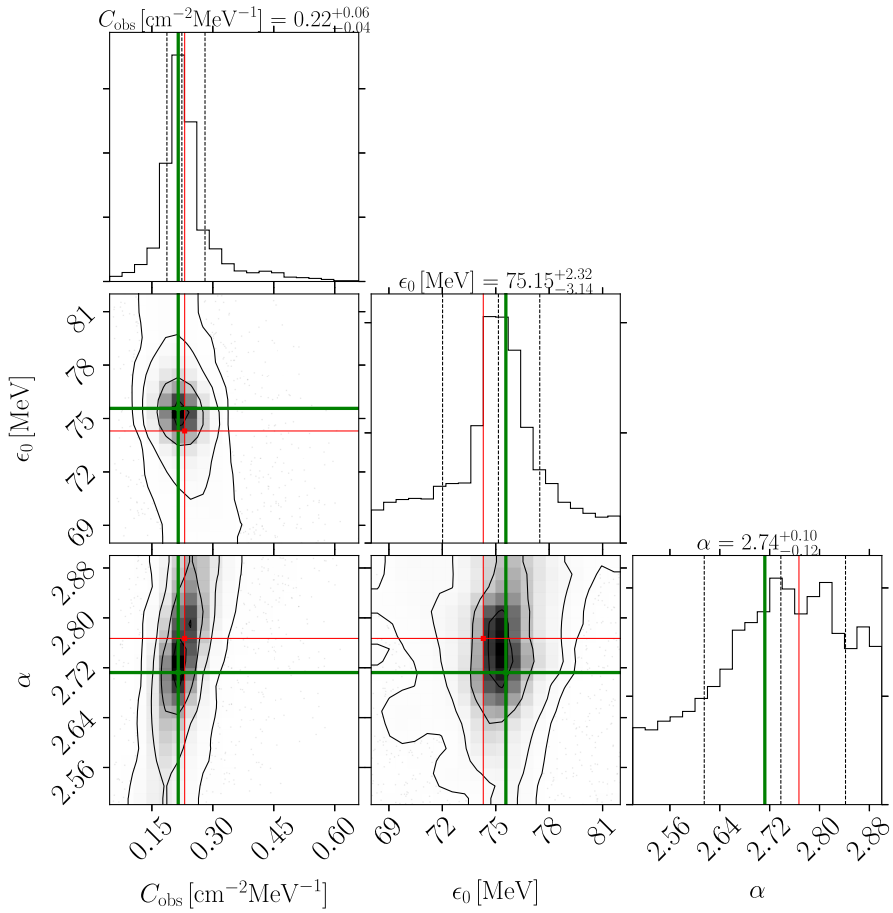


FIG. 7. Best-fitting values and posterior distributions of the reconstructed time-integrated ALP spectral parameters $C_{\rm obs}, \epsilon_0$ and $\alpha$ for an ALP-induced gamma-ray burst of a future SN of an $11.2M_\odot$ stellar progenitor characterized by $m_a = 0.1$ neV, $g_{a\gamma} = 1.5 \times 10^{-12}$ GeV$^{-1}$. We overlay the marginal two-dimensional posterior distributions with the parameter values used to simulate the mock signal in red, while the green values denote the parameter values maximizing Eq. (18). The marginal one-dimensional posterior distributions for each parameter show the 16%, 50% (median) and 84% quantiles as dashed black lines, whose numerical values are also stated in the title of each marginal posterior.

spectral parameters. In Fig. 7 we display the case of $g_{a\gamma} = 1.5 \times 10^{-12}$ GeV$^{-1}$ as an example of the parameter inference results. We find that in all considered scenarios the parameters $\epsilon_0$ and $\alpha$ are reconstructed with a relative uncertainty not higher than ∼10%. From the results of the statistical analysis shown in Fig. 7, for sake of simplicity, we symmetrize the errors on the flux normalization obtaining the results presented in Table I. Although the marginal posterior distribution of $C_{\rm obs}$ is asymmetric, we adopt the standard deviation of the obtained posterior samples as the proxy for the error on $C_{\rm obs}$. This procedure underestimates the uncertainty on $g_{a\gamma}$ induced by the statistical inference of the spectral parameters of the burst. Yet, as we shall see, the uncertainty on the Galactic magnetic field induces a much larger variance so that our approximation does not strongly bias the final results in Table I.

The observed time-integrated photon flux is fitted by Eq. (14) where the normalization $C_{\rm obs}$ can be conveniently expressed as

$$C_{\rm obs} = \left(\frac{g_{a\gamma}}{g_{a\gamma,0}}\right)^4 \left(\frac{B}{B_0}\right)^2 \frac{C_0}{4\pi L^2} P_{a\gamma,0}. \tag{21}$$

Here, the reference coupling is $g_{a\gamma,0} = 10^{-12}$ GeV$^{-1}$, $C_0 \equiv C(M = 11.2M_\odot)$ from Eq. (4), and the conversion

TABLE I. Reconstructed (Rec.) ALP-photon coupling with associated error bars (third column, see text for detailed derivation) for different values of the input ALP-photon coupling (first column), leading to different values of $C_{\rm obs}$ (second column).

| Input $g_{a\gamma}(\times 10^{-12}$ GeV$^{-1})$ | $C_{\rm obs}$(MeV$^{-1}$ cm$^{-2}$) | Rec. $g_{a\gamma}(\times 10^{-12}$ GeV$^{-1})$ |
|---|---|---|
| 1.00 | $0.042 \pm 0.007$ | $0.90^{+0.76}_{-0.25}$ |
| 1.50 | $0.221 \pm 0.026$ | $1.37^{+1.12}_{-0.36}$ |
| 2.00 | $0.727 \pm 0.083$ | $1.84^{+1.50}_{-0.48}$ |
| 2.50 | $1.718 \pm 0.186$ | $2.30^{+1.87}_{-0.60}$ |
| 3.00 | $3.758 \pm 0.384$ | $2.78^{+2.25}_{-0.72}$ |

probability $P_{a\gamma,0} = P_{a\gamma}(g_{a\gamma,0}, B_0) = 7.813 \times 10^{-5}$ is calculated for this given reference coupling and a benchmark magnetic field model characterized by an average transverse magnetic field $B_0 = 0.58$ μG along the line of sight. This value is obtained by considering the "JFnew" model discussed in Sec. II. In Table I, we report the inferred values of the burst normalization $C_{\rm obs}$ for all five cases. As expected, the relative uncertainty depends on the total luminosity of the observed burst. Here we note that the central value of the reconstructed $g_{a\gamma}$ is systematically smaller than the real one. This is due to the fact that the fit in Eq. (4) overestimates the ALP production in the SN for the considered $11.2M_\odot$ model (see also Fig. 3 in [15]).

Inverting Eq. (21), it is possible to reconstruct the ALP-photon coupling for different values of the assumed real value of the coupling. The uncertainty on the reconstructed $g_{a\gamma}$ is related to the experimental uncertainty on $C_{\rm obs}$ and the theoretical one on $C_0$ as

$$\frac{\delta g_{a\gamma}}{g_{a\gamma}} = \frac{1}{4}\left(\frac{\delta C_{\rm obs}}{C_{\rm obs}} + \frac{\delta C_0}{C_0}\right), \tag{22}$$

assuming that the distance $L$ is accurately known. For the Galactic magnetic field we consider the 3 different models discussed in Sec. II C. The variability related to the different magnetic field models is much larger than the uncertainty evaluated in Eq. (22) fixing the magnetic field. In Eq. (21) $B$ is evaluated as in Eq. (11) along the line of sight and with $B_0 = 0.58$ μG the benchmark value taken from the "JFnew" model.

In Table II we show the values of the reconstructed $g_{a\gamma}$ for input value $g_{a\gamma} = 1.5 \times 10^{-12}$ GeV$^{-1}$, assuming different magnetic field models. The three models of magnetic field discussed in Sec. II C are listed in decreasing order for the value of the average transverse magnetic field $B$ (second column). Clearly, the higher the assumed magnetic field, the lower the reconstructed $g_{a\gamma}$. The Galactic magnetic field is known to be described by the "JFnew" model and, if we are confident of this assumption, the uncertainty on $g_{a\gamma}$ goes down to ±15%. Conservatively, we associate the uncertainty on the reconstructed coupling to the entire range of variability for the three magnetic field models. The smallest $g_{a\gamma}$ is obtained with the "JF" model and the biggest one with the "Psh" model. These two extreme values give rise to the uncertainty band on the reconstructed $g_{a\gamma}$.

TABLE II. Reconstructed (Rec.) ALP-photon coupling (third column) for different choices of the Galactic magnetic field model (first column), with average values along the line of sight given in the second column. These values refer to a real coupling $g_{a\gamma} = 1.5 \times 10^{-12}$ GeV$^{-1}$.

| Model | $B$(μG) | Rec. $g_{a\gamma}$($\times 10^{-12}$ GeV$^{-1}$) |
|---|---|---|
| "JF" | 0.76 | $1.19 \pm 0.19$ |
| "JFnew" | 0.58 | $1.37 \pm 0.21$ |
| "Psh" | 0.235 | $2.15 \pm 0.33$ |

Following this approach, in Table I we show the reconstructed ALP-photon coupling with the associated error bars (third column) for different values of the "real" $g_{a\gamma}$ (first column), corresponding to a given $C_{\rm obs}$ (second column). The large uncertainty on the magnetic field leads to a ∼2 factor uncertainty on the reconstructed ALP-photon coupling. For clarity, this table can be compared with Table II, noticing that the mean value of $g_{a\gamma}$ corresponds to the "JFnew" model, which is the most realistic one, and the asymmetric $1\sigma$ error bars are given by the lowest coupling reconstructed with the "JF" model and the highest one obtained with the "Psh" model. In Fig. 6 we show the reconstructed ALP-photon coupling (the dashed blue line) with the $1\sigma$ band error associated with the uncertainty on the modeling of the Galactic magnetic field for the benchmark case $m_a = 0.1$ neV and $g_{a\gamma} = 1.5 \times 10^{-12}$ GeV$^{-1}$. In case of such an observation, the coupling would be reconstructed within a factor two due to the uncertainties on the Galactic magnetic field. On the other hand, a measurement would not reveal any information on the ALP mass. However, for the considered coupling, the strong astrophysical bounds robustly exclude $m_a \lesssim 10^{-11}$ eV. Thus, given the critical mass discussed in Sec. II D, the observation of an ALP-induced gamma-ray signal in combination with other constraints would allow one to infer an ALP mass 0.01 neV $\lesssim m_a \lesssim \mathcal{O}(0.1)$ neV.

### C. ALP parameter reconstruction for $m_a \gtrsim m_a^c$

As discussed in Sec. II, the reconstruction of the ALP-photon coupling in the massive case is less straightforward since the result depends on the unknown ALP mass.

#### *1. Intermediate mass range*

In the intermediate ALP mass range $m_a \approx m_a^c$, the reconstruction of the ALP properties is unfeasible given the performance metrics of the Fermi-LAT. Indeed, the ALP-mass induced modulation of the spectrum is almost completely washed out by the poor energy resolution of the detector at these energies. We give a qualitative impression of the impact of the LAT energy dispersion on the modulated time-integrated gamma-ray burst spectrum in the left panel of Fig. 8. We illustrate the impact of the LAT energy resolution via a qualitative[6] comparison between a simulated ALP burst spectrum (averaged over 200 Poisson realizations) that includes (solid lines) and neglects (dashed lines) the effect of the instrument (irreducible) energy dispersion for the case of $m_a = 1$ neV. The impact of the ALP mass is clearly visible for the spectra without energy dispersion, even in this rather coarse binning for a

[6]The chosen spectral binning in Fig. 8 is much finer than the LAT energy resolution would allow for at these energies.

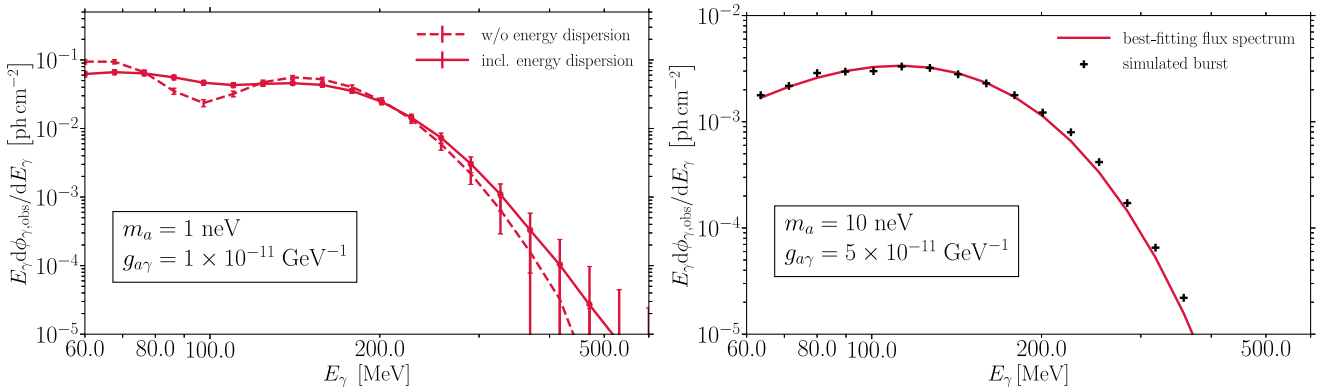


FIG. 8. Left panel: Simulated gamma-ray spectra between 60 MeV to 600 MeV split in 20 logarithmically spaced energy bins of an ALP burst originating in a CC SN with the benchmark characteristics detailed in Sec. III A. The spectra are generated for an ALP mass of $m_a = 1$ neV and $g_{a\gamma} = 10^{-11}$ GeV$^{-1}$. For definiteness, we fix $\beta = 2.77$, $E_0 = 74.3$ MeV as the ALP burst spectrum according to the parametrization in Eq. (3). To illustrate the impact of the LAT energy resolution, we distinguish the case with full implementation of the energy dispersion matrix (solid lines) and without any energy dispersion (dashed lines). The error bars indicate the statistical uncertainty due to the Poisson nature of the measurement. The displayed spectra are averaged over 200 Poisson realizations of the signal. Right panel: Simulated flux spectrum of a gamma-ray burst induced by ALPs of mass $m_a = 10$ neV and ALP-photon coupling $g_{a\gamma} = 5 \times 10^{-11}$ GeV$^{-1}$ produced by the same SN stellar progenitor. Black crosses represent the simulated data points, and the red curve represents the fit function based on the analytic description given in Eq. (14). The results have been derived with a $\chi^2$-fit applying the prescription in Eq. (23), leading to $\alpha = 4.2$ and $\epsilon_0 = 112$ MeV.

spectral modulation study. This feature is almost completely washed out after including the energy dispersion of Fermi-LAT.

### 2. Large mass range

The $m_a \gg m_a^c$ regime can be distinguished from the massless case through the measured value of the $\alpha$ parameter. As discussed in Sec. II D and illustrated in Fig. 5, the spectral index in this case is much larger than 2. We verify that the results of these analytic considerations are retained in a fit to simulated data, i.e. using the correct LAT instrument response function. To this end, we slightly modify the statistical approach of Sec. III C:

(i) We derive the time-integrated flux spectrum of the gamma-ray burst $\boldsymbol{n}$ by dividing the simulated photon counts by the exposure per energy bin (utilizing `gtexposure`).
(ii) We obtain the flux $\boldsymbol{S}$ from the fit formula in Eq. (14) by integration in energy and directly fit its parameters to the observed burst flux.
(iii) We perform a $\chi^2$-fit with correlated errors based on the covariance matrix $K$ as defined before but now representing flux uncertainties. Namely, we minimize the function:

$$\chi^2 = (\boldsymbol{n} - \boldsymbol{S})^T K^{-1} (\boldsymbol{n} - \boldsymbol{S}). \tag{23}$$

In contrast to the case of $m_a = 10$ neV presented in Fig. 5, we select a larger ALP-photon coupling $g_{a\gamma} = 5 \times 10^{-11}$ GeV$^{-1}$ to ensure enough statistics. We stress that this coupling strength is already excluded by multiple independent probes so that our results simply showcase what could be done in reality with sufficient statistics. For smaller values of $g_{a\gamma}$, not excluded by other arguments, the statistics is poorer and the reconstruction of the ALP parameters would be more uncertain.

In the right panel of Fig. 8 we show the results of the $\chi^2$-fit, which yields the best-fitting parameters $\alpha = 4.2$ and $\epsilon_0 = 112$ MeV. The spectral index of $\alpha = 4.2$ confirms the prediction of Sec. II D, i.e. in the massive case we expect a substantially larger value of the spectral index than for $m_a \ll m_a^c$. We emphasize that the derived best-fitting values are subject to large uncertainties of the order of the obtained value itself. Thus, though the value of the spectral index can be considered a good indicator of an ALP of mass *above a few neV*, the spectral analysis of the observed gamma-ray burst remains a challenging task.

## V. CONCLUSIONS

In this paper we investigated the possibility of detecting ALPs produced in a nearby SN explosion through their conversion into gamma rays. One may wonder if long GRBs, lasting more than 2 s and partially falling in the same energy range of the ALP-induced signal, could contaminate this signal. Indeed, core-collapse SNe are expected to generate long GRBs associated with jet emission. However, GRB signals are delayed on the order of tens of seconds to minutes with respect to the core collapse [56,57], tagged by the neutrino emission. The origin of such a delay is related to the time needed by the jet to form and propagate through the SN envelope, leading to

the GRB production. Therefore, the only source of standard background for the ALP-induced signal would be the gamma-ray emission in the pre-jet phase, whose mechanism is currently poorly understood. In this context, different theoretical models have been proposed to address the origin of such a precursor emission, including photospheric emission model, minijets, geometrically thin shells and magnetic reconnection [58–61], featuring temporal and spectral differences. In particular, some models predict a thermal spectrum with average photon energy of ∼1 MeV with a time delay of less than 10 s from the core collapse (see, e.g., Refs. [58,60]). For a Galactic SN this emission may lead to an isotropic component of high-energy gamma rays, which might fall within the time envelope of the observed neutrino signal. However, given the small amount of observational data, the origin and the properties of such a precursor emission are still under debate [58–61]. Therefore, here we have assumed that the ALP-induced signal is not contaminated by any standard physics background and the observed gamma-ray signal would be a hint of new physics. The theoretical framework behind the production and propagation of ALPs has been discussed, and the potential for their detection through the Fermi-LAT has been investigated.

By considering, as a benchmark, a Galactic core-collapse SN at 10 kpc from Earth, we computed the sensitivity reach of the LAT to be $g_{a\gamma} \simeq 4 \times 10^{-13}$ GeV$^{-1}$ in the mass range $m_a \lesssim \mathcal{O}(0.1)$ neV. This value can vary by a factor of 2 depending on the magnetic field configuration which represents the largest model uncertainty at play, see discussion in Sec. II.

By fully simulating the ALP-induced gamma-ray burst signal with the LAT, we studied how the ALP parameters can be reconstructed from the analysis of gamma-ray data. We identified three mass ranges which require two different analysis approaches. In particular, in the low-mass regime, and high-mass regime, a fit of the gamma-ray signal with the gamma distribution in Eq. (14) can inform us about fundamental properties of the ALPs. When the ALPs are lighter than $\mathcal{O}(0.1)$ neV, the reconstruction of the ALP parameters can be very precise, with errors of order 15%. Including the variation of the reconstructed parameters because of magnetic field uncertainties, one can reconstruct $g_{a\gamma}$ with errors of about a factor 2. In case of the observation of an ALP-induced photon signal, the interplay with other astrophysical constraints would suggest an ALP mass $0.01\ \text{neV} \lesssim m_a \lesssim \mathcal{O}(0.1)$ neV. We also demonstrated that a value of the spectral index $\alpha \sim 4$ will be a good indicator of an ALP with mass above a few neV.

The results show that a detection of such a signal would provide a unique opportunity to probe the properties of ALPs and shed new light on fundamental physics. Here we considered only the case of ALPs coupled with photons but the approach discussed in this work can be easily generalized to ALPs with other interactions, for example to the case of ALPs produced by processes involving nucleons [62–65]. The detection of gamma-ray signals from SN explosions has been a major topic of interest in astrophysics for several decades, and the potential detection of ALPs adds a new dimension to this field. This study highlights the importance of continued research in this area and the potential for exciting new discoveries in the future.

## ACKNOWLEDGMENTS

We thank Milena Crnogorčević, Manuel Meyer and Edoardo Vitagliano for useful discussions. This article is based upon work from COST Action COSMIC WISPers CA21106, supported by COST (European Cooperation in Science and Technology). This work has been done thanks to the facilities offered by the Univ. Savoie Mont Blanc—CNRS/IN2P3 MUST computing center. This work is (partially) supported by ICSC—Centro Nazionale di Ricerca in High Performance Computing, Big Data and Quantum Computing, funded by European Union—NextGenerationEU. The work of P. C. is supported by the European Research Council under Grant No. 742104 and by the Swedish Research Council (VR) under Grants No. 2018-03641 and No. 2019-02337. The work of C. E. is supported by the "Agence Nationale de la Recherche" through Grant No. ANR-19-CE31-0005-01 (PI: F. Calore). The work of C. E. has been supported by the EOSC Future project which is cofunded by the European Union Horizon Programme call INFRAEOSC-03-2020, Grant Agreement No. 101017536. The work of A. M. and G. L. is partially supported by the Italian Istituto Nazionale di Fisica Nucleare (INFN) through the "Theoretical Astroparticle Physics" project and by the research Grant No. 2017W4HA7S "NAT-NET: Neutrino and Astroparticle Theory Network" under the program PRIN 2017 funded by the Italian Ministero dell'Università e della Ricerca (MUR). P. C., M. G. and G. L. thank the Galileo Galilei Institute for Theoretical Physics for hospitality during the preparation of part of this work.

[1] J. A. Grifols, E. Masso, and R. Toldra, Gamma-rays from SN1987A due to pseudoscalar conversion, Phys. Rev. Lett. **77**, 2372 (1996).

[2] J. W. Brockway, E. D. Carlson, and G. G. Raffelt, SN1987A gamma-ray limits on the conversion of pseudoscalars, Phys. Lett. B **383**, 439 (1996).

[3] A. Payez, C. Evoli, T. Fischer, M. Giannotti, A. Mirizzi, and A. Ringwald, Revisiting the SN1987A gamma-ray limit on ultralight axion-like particles, J. Cosmol. Astropart. Phys. 02 (2015) 006.

[4] J. Jaeckel, P. C. Malta, and J. Redondo, Decay photons from the axionlike particles burst of type II supernovae, Phys. Rev. D **98**, 055032 (2018).

[5] F. Calore, P. Carenza, M. Giannotti, J. Jaeckel, and A. Mirizzi, Bounds on axionlike particles from the diffuse supernova flux, Phys. Rev. D **102**, 123005 (2020).

[6] A. Caputo, G. Raffelt, and E. Vitagliano, Muonic boson limits: Supernova redux, Phys. Rev. D **105**, 035022 (2022).

[7] S. Hoof and L. Schulz, Updated constraints on axion-like particles from temporal information in supernova SN1987A gamma-ray data, J. Cosmol. Astropart. Phys. 03 (2023) 054.

[8] E. Müller, F. Calore, P. Carenza, C. Eckner, and M. C. D. Marsh, Investigating the gamma-ray burst from decaying MeV-scale axion-like particles produced in supernova explosions, J. Cosmol. Astropart. Phys. 07 (2023) 056.

[9] L. Oberauer, C. Hagner, G. Raffelt, and E. Rieger, Supernova bounds on neutrino radiative decays, Astropart. Phys. **1**, 377 (1993).

[10] G. M. Fuller, A. Kusenko, and K. Petraki, Heavy sterile neutrinos and supernova explosions, Phys. Lett. B **670**, 281 (2009).

[11] C. A. Argüelles, V. Brdar, and J. Kopp, Production of keV sterile neutrinos in supernovae: New constraints and gamma ray observables, Phys. Rev. D **99**, 043012 (2019).

[12] W. DeRocco, P. W. Graham, D. Kasen, G. Marques-Tavares, and S. Rajendran, Observable signatures of dark photons from supernovae, J. High Energy Phys. 02 (2019) 171.

[13] M. Meyer, M. Giannotti, A. Mirizzi, J. Conrad, and M. A. Sánchez-Conde, Fermi large area telescope as a galactic supernovae axionscope, Phys. Rev. Lett. **118**, 011103 (2017).

[14] M. Meyer and T. Petrushevska, Search for axionlike-particle-induced prompt $\gamma$-ray emission from extragalactic core-collapse supernovae with the Fermi Large Area Telescope, Phys. Rev. Lett. **124**, 231101 (2020); **125**, 119901(E) (2020).

[15] F. Calore, P. Carenza, C. Eckner, T. Fischer, M. Giannotti, J. Jaeckel, K. Kotake, T. Kuroda, A. Mirizzi, and F. Sivo, 3D template-based Fermi-LAT constraints on the diffuse supernova axion-like particle background, Phys. Rev. D **105**, 063028 (2022).

[16] G. Raffelt and L. Stodolsky, Mixing of the photon with low mass particles, Phys. Rev. D **37**, 1237 (1988).

[17] A. Mezzacappa and S. W. Bruenn, A numerical method for solving the neutrino Boltzmann equation coupled to spherically symmetric stellar core collapse, Astrophys. J. **405**, 669 (1993).

[18] M. Liebendoerfer, O. E. B. Messer, A. Mezzacappa, S. W. Bruenn, C. Y. Cardall, and F. K. Thielemann, A finite difference representation of neutrino radiation hydrodynamics for spherically symmetric general relativistic supernova simulations, Astrophys. J. Suppl. Ser. **150**, 263 (2004).

[19] A. Burrows, L. Dessart, E. Livne, C. D. Ott, and J. Murphy, Simulations of magnetically-driven supernova and hypernova explosions in the context of rapid rotation, Astrophys. J. **664**, 416 (2007).

[20] J. Matsumoto, T. Takiwaki, K. Kotake, Y. Asahina, and H. R. Takahashi, 2D numerical study for magnetic field dependence of neutrino-driven core-collapse supernova models, Mon. Not. R. Astron. Soc. **499**, 4174 (2020).

[21] P. Mösta, C. D. Ott, D. Radice, L. F. Roberts, E. Schnetter, and R. Haas, A large scale dynamo and magnetoturbulence in rapidly rotating core-collapse supernovae, Nature (London) **528**, 376 (2015).

[22] M. Obergaulinger and M.-A. Aloy, Magnetorotational core collapse of possible GRB progenitors. III. Three-dimensional models, Mon. Not. R. Astron. Soc. **503**, 4942 (2021).

[23] E. Guarini, P. Carenza, J. Galan, M. Giannotti, and A. Mirizzi, Production of axionlike particles from photon conversions in large-scale solar magnetic fields, Phys. Rev. D **102**, 123024 (2020).

[24] A. Caputo, A. J. Millar, and E. Vitagliano, Revisiting longitudinal plasmon-axion conversion in external magnetic fields, Phys. Rev. D **101**, 123004 (2020).

[25] A. Caputo, P. Carenza, G. Lucente, E. Vitagliano, M. Giannotti, K. Kotake, T. Kuroda, and A. Mirizzi, Axionlike particles from hypernovae, Phys. Rev. Lett. **127**, 181102 (2021).

[26] A. De Angelis, G. Galanti, and M. Roncadelli, Relevance of axion-like particles for very-high-energy astrophysics, Phys. Rev. D **84**, 105030 (2011); **87**, 109903(E) (2013).

[27] D. Horns, L. Maccione, M. Meyer, A. Mirizzi, D. Montanino, and M. Roncadelli, Hardening of TeV gamma spectrum of AGNs in galaxy clusters by conversions of photons into axion-like particles, Phys. Rev. D **86**, 075024 (2012).

[28] P. Carenza, C. Evoli, M. Giannotti, A. Mirizzi, and D. Montanino, Turbulent axion-photon conversions in the Milky Way, Phys. Rev. D **104**, 023003 (2021).

[29] R. Jansson and G. R. Farrar, A new model of the galactic magnetic field, Astrophys. J. **757**, 14 (2012).

[30] B. Gold *et al.*, Seven-year Wilkinson microwave anisotropy probe (WMAP) observations: Galactic foreground emission, Astrophys. J. Suppl. Ser. **192**, 15 (2011).

[31] R. Adam *et al.* (Planck Collaboration), Planck intermediate results.: XLII. Large-scale Galactic magnetic fields, Astron. Astrophys. **596**, A103 (2016).

[32] R. Adam *et al.* (Planck Collaboration), Planck 2015 results. I. Overview of products and scientific results, Astron. Astrophys. **594**, A1 (2016).

[33] P. A. R. Ade *et al.* (Planck Collaboration), Planck 2015 results—II. Low Frequency Instrument data processings, Astron. Astrophys. **594**, A2 (2016).

[34] P. A. R. Ade *et al.* (Planck Collaboration), Planck 2015 results. VI. LFI mapmaking, Astron. Astrophys. **594**, A6 (2016).

[35] M. S. Pshirkov, P. G. Tinyakov, P. P. Kronberg, and K. J. Newton-McGee, Deriving global structure of the galactic

magnetic field from Faraday rotation measures of extragalactic sources, Astrophys. J. **738**, 192 (2011).
[36] P. P. Kronberg and K. J. Newton-McGee, Remarkable symmetries in the Milky Way disk's magnetic field, Pub. Astron. Soc. Aust. **28**, 171 (2011).
[37] A. Mirizzi, G. G. Raffelt, and P. D. Serpico, Signatures of axion-like particles in the spectra of TeV gamma-ray sources, Phys. Rev. D **76**, 023001 (2007).
[38] M. C. D. Marsh, J. H. Matthews, C. Reynolds, and P. Carenza, Fourier formalism for relativistic axion-photon conversion with astrophysical applications, Phys. Rev. D **105**, 016013 (2022).
[39] W. B. Atwood *et al.*, The large area telescope on the fermi gamma-ray space telescope mission, Astrophys. J. **697**, 1071 (2009).
[40] G. J. Feldman and R. D. Cousins, A unified approach to the classical statistical analysis of small signals, Phys. Rev. D **57**, 3873 (1998).
[41] F. Halzen and G. G. Raffelt, Reconstructing the supernova bounce time with neutrinos in IceCube, Phys. Rev. D **80**, 087301 (2009).
[42] H. Dembinski, P. Ongmongkolkul *et al.*, scikit-hep/iminuit, 10.5281/zenodo.3949207 (2020).
[43] F. Feroz, M. P. Hobson, and M. Bridges, MultiNest: An efficient and robust Bayesian inference tool for cosmology and particle physics, Mon. Not. R. Astron. Soc. **398**, 1601 (2009).
[44] C. S. Reynolds, M. C. D. Marsh, H. R. Russell, A. C. Fabian, R. Smith, F. Tombesi, and S. Veilleux, Astrophysical limits on very light axion-like particles from Chandra grating spectroscopy of NGC 1275, Astrophys. J. **890**, 59 (2020).
[45] C. Dessert, J. W. Foster, and B. R. Safdi, X-ray searches for axions from super star clusters, Phys. Rev. Lett. **125**, 261102 (2020).
[46] D. Noordhuis, A. Prabhu, S. J. Witte, A. Y. Chen, F. Cruz, and C. Weniger, Novel constraints on axions produced in pulsar polar cap cascades, Phys. Rev. Lett. **131**, 111004 (2023).
[47] C. Dessert, D. Dunsky, and B. R. Safdi, Upper limit on the axion-photon coupling from magnetic white dwarf polarization, Phys. Rev. D **105**, 103034 (2022).
[48] C. O'Hare, cajohare/axionlimits: Axionlimits, 10.5281/zenodo.3932430 (2020).
[49] M. Escudero, C. K. Pooni, M. Fairbairn, D. Blas, X. Du, and D. J. E. Marsh, Axion star explosions: A new source for axion indirect detection, arXiv:2302.10206.
[50] S. Al Kharusi *et al.* (SNEWS Collaboration), SNEWS 2.0: A next-generation supernova early warning system for multi-messenger astronomy, New J. Phys. **23**, 031201 (2021).
[51] R. Adam *et al.* (Planck Collaboration), Planck intermediate results. XLVII. Planck constraints on reionization history, Astron. Astrophys. **596**, A108 (2016).
[52] N. Aghanim *et al.* (Plack Collaboraton), Planck 2018 results. VI. Cosmological parameters, Astron. Astrophys. **641**, A6 (2020); **652**, C4(E) (2021).
[53] P. Mocz, M. Vogelsberger, V. H. Robles, J. Zavala, M. Boylan-Kolchin, A. Fialkov, and L. Hernquist, Galaxy formation with BECDM—I. Turbulence and relaxation of idealized haloes, Mon. Not. R. Astron. Soc. **471**, 4559 (2017).
[54] M. Nori and M. Baldi, Scaling relations of fuzzy dark matter haloes—I. Individual systems in their cosmological environment, Mon. Not. R. Astron. Soc. **501**, 1539 (2021).
[55] M. Mina, D. F. Mota, and H. A. Winther, Solitons in the dark: First approach to non-linear structure formation with fuzzy dark matter, Astron. Astrophys. **662**, A29 (2022).
[56] S. E. Woosley, Models for gamma-ray burst progenitors and central engines, arXiv:1105.4193.
[57] M. Crnogorčević, R. Caputo, M. Meyer, N. Omodei, and M. Gustafsson, Searching for axionlike particles from core-collapse supernovae with Fermi LAT's low-energy technique, Phys. Rev. D **104**, 103001 (2021).
[58] M. Lyutikov and V. Usov, Precursors of gamma-ray bursts: A clue to the burster's nature, Astrophys. J. Lett. **543**, L129 (2000).
[59] A. I. MacFadyen, S. E. Woosley, and A. Heger, Supernovae, jets, and collapsars, Astrophys. J. **550**, 410 (2001).
[60] X.-Y. Wang and P. Meszaros, GRB precursors in the fallback collapsar scenario, Astrophys. J. **670**, 1247 (2007).
[61] G. V. Lipunova, E. S. Gorbovskoy, A. I. Bogomazov, and V. M. Lipunov, Population synthesis of gamma-ray bursts with precursor activity and the spinar paradigm, Mon. Not. R. Astron. Soc. **397**, 1695 (2009).
[62] P. Carenza, T. Fischer, M. Giannotti, G. Guo, G. Martínez-Pinedo, and A. Mirizzi, Improved axion emissivity from a supernova via nucleon-nucleon bremsstrahlung, J. Cosmol. Astropart. Phys. 10 (2019) 016; 05 (2020) E01.
[63] P. Carenza, B. Fore, M. Giannotti, A. Mirizzi, and S. Reddy, Enhanced supernova axion emission and its implications, Phys. Rev. Lett. **126**, 071102 (2021).
[64] A. Lella, P. Carenza, G. Lucente, M. Giannotti, and A. Mirizzi, Protoneutron stars as cosmic factories for massive axionlike particles, Phys. Rev. D **107**, 103017 (2023).
[65] A. Lella, P. Carenza, G. Co', G. Lucente, M. Giannotti, A. Mirizzi, and T. Rauscher, Getting the most on supernova axions, Phys. Rev. D **109**, 023001 (2024).